Int. J. Heat Mass Transfer. Vol. 34, No. 9, pp. 2409–2421, 1991
Printed in Great Britain

0017–9310/91 $3.00 + 0.00


# Time-dependent double diffusion in a stably stratified fluid under lateral heating

JIN WOOK LEE and JAE MIN HYUN†

Department of Mechanical Engineering, Korea Advanced Institute of Science and Technology, P.O. Box 150, Cheong Ryang, Seoul, Korea

(*Received* 15 *May* 1990 *and in final form* 23 *October* 1990)

**Abstract**—A numerical study is made of double diffusive convection in a rectangle. The fluid is initially at rest with a pre-existing stably stratified solutal gradient. The motion is initiated by abruptly raising the temperature at one vertical sidewall. Comprehensive and systematically-organized numerical solutions to the full, Navier–Stokes equations under the Boussinesq fluid assumption have been acquired. Far-reaching analyses are made of the numerical results over a wide range of the solutal Rayleigh numbers $R_s$ using the thermal Rayleigh number, $R_t = 10^7$. Elaborate plots displaying the details of the evolutions of the flow, temperature and solutal fields in the cavity are presented. The vertical profiles of the velocity, temperature, solute, and the local Nusselt number are constructed, delineating the influence of solutal buoyancy effect relative to the thermal effect. The behaviour of the details of the computed flow characteristics is in good qualitative agreement with the available experimental visualizations. The categorization of the basic character of the flow into the supercritical ($Ra > Ra_c$) and subcritical regimes ($Ra < Ra_c$), which is based on experimental observations, is satisfactorily verified by the numerical results. The present numerical simulations are also supportive of the prior observations, which illustrated the qualitative difference in the time-dependent patterns of the formation of the layered structure in the supercritical and subcritical regimes. By assessing the present numerical results, the previous estimate of the value of $Ra_c \cong 1.5 \times 10^4$ is found to be reasonably accurate.

## 1. INTRODUCTION

THE STUDY of double diffusive convective motions in confined spaces has received considerable attention in recent years. Much of the efforts have been directed toward analysing the laboratory flow models which are formulated in enclosures of geometrically simple configurations, mostly in rectangular cavities. Of particular concern are various flow models that have relevance to applications to the oceanic flow processes; the common diffusing agents are therefore heat and salt (or some other dissolved substance). The fundamental aspects of the general subject of double diffusive convection have eloquently been reviewed (e.g. see Turner [1, 2], and Huppert and Turner [3]).

One of the striking characteristics of double diffusive convection in an enclosure is the formation of layers, separated by thin interfaces, under appropriate conditions. Especially, the emergence of well-mixed horizontal layers in a stably stratified fluid, by way of convective motions, has been an issue of much interest. Turner [4], by heating from below a confined fluid having a statically stable salinity gradient, succinctly illustrated the layered structure. He estimated the growth rate of the first layer adjacent to the heated bottom. His theoretical and experimental investigations also provided the criteria for the formation of the successive layers above the first. Incropera and Viskanta [5], using salt stratified solutions, examined the flow heated from below for the cases of two different bottom wall conditions, i.e. a uniform surface temperature and a uniform heat flux at the bottom wall. It was seen that the secondary layers were developed when the thermal forcing at the bottom boundary satisfied certain restrictive conditions.

The above-cited works dealt with the flows when the heating was applied at the bottom of the container. Another important form of the thermal boundary condition is heating at the sidewall, thereby creating a system-wide horizontal temperature gradient applied across the container width. This type of thermal forcing is of great help to a host of modern technological applications. As observed by Ostrach [6], essential elements of the heat and fluid transport phenomena that occur in materials processing involve double diffusive convection subjected to lateral heating. Spurred by such practical needs and motivated by a desire to deepen our basic understanding, several recent accounts addressed the principal character of the flow when heating was applied at a vertical sidewall boundary of the vessel (see, e.g. Thorpe *et al.* [7], Suzukawa and Narusawa [8] and Tanny and Tsinober [9]). It has been established that lateral heating can also produce the layered structure in a solution with a pre-existing vertical solute gradient. These experimental studies showed that instability takes place in the form of a system of roll-cells; however, one crucial question is whether these roll-cells are formed simultaneously or successively along the heated sidewall. The classical experiments of Thorpe *et al.* [7] were conducted by using a thin vertical slot. The experimental

† Author to whom all correspondence should be addressed.

## NOMENCLATURE

$Ar$ aspect ratio, $H/L$
$C_h$ dimensional concentration at the high-concentration bottom wall
$C_l$ dimensional concentration at the low-concentration top wall
$c$ non-dimensional layer thickness, $h/\eta$
$\Delta C$ concentration difference at initial state, $C_h - C_l$
$D$ mass diffusivity
$g$ gravity
$H$ height of cavity
$h$ layer thickness observed in numerical result
$L$ width of cavity
$Le$ Lewis number, $\kappa/D$
$Nu$ local Nusselt number
$P$ non-dimensional pressure
$p$ dimensional pressure
$Pr$ Prandtl number, $\nu/\kappa$
$Ra$ effective Rayleigh number, $g\beta_t\Delta\theta\eta^3/\kappa\nu$
$R_s$ solutal Rayleigh number, $g\beta_s\Delta C L^3/\kappa\nu$
$R_t$ thermal Rayleigh number, $g\beta_t\Delta\theta L^3/\kappa\nu$
$R_\rho$ buoyancy ratio, $\beta_s\Delta C/\beta_t\Delta\theta$
$S$ non-dimensional concentration
$T$ non-dimensional temperature
$t$ dimensional time
$U$ non-dimensionalized horizontal velocity component
$u$ dimensional horizontal velocity component
$V$ non-dimensionalized vertical velocity component
$v$ dimensional vertical velocity component
$X$ non-dimensional horizontal coordinate
$x$ dimensional horizontal coordinate
$Y$ non-dimensional vertical coordinate
$y$ dimensional vertical coordinate.

Greek symbols

$\beta_s$ coefficient of volumetric expansion with concentration
$\beta_t$ coefficient of volumetric expansion with temperature
$\eta$ reference layer thickness
$\theta_h$ dimensional temperature at the high-temperature sidewall
$\theta_l$ dimensional temperature at the low-temperature sidewall
$\Delta\theta$ temperature difference, $\theta_h - \theta_l$
$\kappa$ thermal diffusivity
$\nu$ kinematic viscosity
$\rho$ dimensional density
$\rho_r$ dimensional reference density
$\tau$ non-dimensional time
$\psi$ non-dimensional stream function.

observations clearly demonstrated the horizontal cells propagating into the interior. However, the predictions based on the concurrent analyses by Thorpe *et al.* exhibited partial inconsistencies with the experimental visualizations. In the experiments, the sense of rotation in all of the cells was the same, whereas in the stability analysis counter-rotating pairs of cells were predicted. Thorpe *et al.* also presented the stability diagram for the onset of the cellular convective motions. Following the original expositions of Thorpe *et al.*, a considerable number of papers have treated the general topics of the flow behaviour in a fluid system as having a stable background vertical solute gradient subject to an externally-imposed horizontal temperature gradient. Hart [10] and Wirtz and Liu [11] were concerned with the onset of cellular convection in a narrow slot. The major results of the stability analysis of Hart [10] and the numerical computations of Wirtz and Liu [11] were in close agreement with the predictions of Thorpe *et al.* [7]. The stream patterns presented by Chen [12] displayed pairs of counter-rotating rolls in an infinite vertical slot, which was the anticipated result since he restricted himself to looking at periodic infinitesimal disturbances to the background state. However, the computations by Thangam *et al.* [13] for an inclined slot showed that the motions in all of the cells had the same sense of rotation.

A decisive and physically insightful argument was advanced by Chen *et al.* [14], who considered similar problems in a relatively wide tank. They pointed out that there exists a characteristic length scale $\eta$, defined as $\eta = [\rho(T_\infty, S_\infty) - \rho(T_w, S_\infty)]/|d\rho/dy|_0$, where $\rho(T, S)$ denotes the density as a function of temperature $T$ and concentration $S$; subscripts $\infty$ and w refer to the conditions in the far field and at the wall, respectively; and $(d\rho/dy)_0$ indicates the pre-existing stable density gradient. Physically, $\eta$ can be interpreted as a measure of the vertical distance that a heated fluid element would rise against the pre-existing background density gradient $(d\rho/dy)_0$. Extending these lines of thoughts, they asserted that a physically meaningful Rayleigh number $Ra$ could be defined by using $\eta$ as the reference length scale. Furthermore, Chen *et al.* [14] emphasized the significance of the critical Rayleigh number $Ra_c$. They gave an estimate $Ra_c \cong 15000 \pm 2500$; when $Ra$ exceeds this value, cellular convection is expected to occur. The experimental work of Huppert and Turner [15] and Huppert *et al.* [16] took measurements of the heights of the layers over a wide range of $Ra$. One notable contention of these investigations was that, beyond a

Rayleigh number of about $10^5$, the non-dimensional cell height $c$, $c = h/\eta$, was essentially independent of the Rayleigh number and $c$ was given an approximate value $c \cong 0.62$ [15] or 0.6 [16].

A perusal of the preceding work clearly reveals that qualitative depictions have been provided for the basic physical mechanisms of the layer structure that arises in a stably stratified fluid due to the lateral heating. The above-mentioned previous studies substantially enhanced our fundamental knowledge of the major dynamic elements. However, at the same time, there also remain some significant inconsistencies as to the details of the flow behaviour. One elusive question is a precise description of the way the cellular patterns are generated and established. Stated alternatively, further explorations are needed to determine whether these cells are formed simultaneously or sequentially, as $Ra$ traverses a wide range encompassing the subcritical ($Ra < Ra_c$) and supercritical ($Ra > Ra_c$) flow regimes. Some of the assertions of the prior reports on the details of the layer structure and the associated thermal and concentration fields need to be verified by other independent investigations.

The purpose of the present study is to perform elaborate numerical calculations of the double diffusive convection in a rectangular cavity. The flow is induced by an impulsively-applied system-wide horizontal temperature gradient in a fluid with a pre-existing statically stable salinity gradient. To date, there are not many comprehensive and full-dress numerical simulations of double diffusive convection under these physical constraints (see, e.g. Wirtz *et al.* [17]). Obviously, extensive numerical computations have the advantage in rendering the precise details of flow evolutions leading to the established layered structure. However, these attempts require excessively large computing resources. These formidable practical difficulties, together with the severity of computational methodologies, have hampered fruitful progress in numerical studies in this field of research. Recently, aided by rapid innovations in computing capabilities, we have secured complete numerical solutions to the full, time-dependent Navier–Stokes equations at high solutal ($R_s$) and thermal ($R_t$) Rayleigh numbers. These numerical results permit precise descriptions of the evolutionary details of the velocity, thermal and solutal fields. Flow characteristics in both the subcritical and supercritical regimes are portrayed. Critical cross-comparisons of the numerical results with the available analytical and experimental data will be conducted. The wealth of flow information obtainable by the present numerical computations illuminates the main character of the flow and helps resolve some of the inconsistencies of the previous endeavours.

## 2. THE MODEL

The full, time-dependent, two-dimensional Navier–Stokes equations, with the Boussinesq-fluid assumption invoked, describe the motions under the present consideration. These equations, expressed in properly non-dimensionalized form and using standard notation, are

$$\frac{\partial U}{\partial X} + \frac{\partial V}{\partial Y} = 0$$

$$\frac{\partial U}{\partial \tau} + \frac{\partial}{\partial X}(UU) + \frac{\partial}{\partial Y}(VU) = -\frac{\partial P}{\partial X} + Pr\left(\frac{\partial^2 U}{\partial X^2} + \frac{\partial^2 U}{\partial Y^2}\right)$$

$$\frac{\partial V}{\partial \tau} + \frac{\partial}{\partial X}(UV) + \frac{\partial}{\partial Y}(VV) = -\frac{\partial P}{\partial Y} + Pr\left(\frac{\partial^2 V}{\partial X^2} + \frac{\partial^2 V}{\partial Y^2}\right) + Pr(R_t T - R_s S)$$

$$\frac{\partial T}{\partial \tau} + \frac{\partial}{\partial X}(UT) + \frac{\partial}{\partial Y}(VT) = \left(\frac{\partial^2 T}{\partial X^2} + \frac{\partial^2 T}{\partial Y^2}\right)$$

$$\frac{\partial S}{\partial \tau} + \frac{\partial}{\partial X}(US) + \frac{\partial}{\partial Y}(VS) = \frac{1}{Le}\left(\frac{\partial^2 S}{\partial X^2} + \frac{\partial^2 S}{\partial Y^2}\right).$$

In the above, the non-dimensional quantities are defined as

$$U = [u/(\kappa/L)], \quad V = [v/(\kappa/L)], \quad X = x/L, \quad Y = y/L, \quad \tau = [t/(L^2/\kappa)],$$

$$P = p/(\rho\kappa^2/L^2), \quad \Delta\theta = \theta_h - \theta_l, \quad \Delta C = C_h - C_l, \quad T = (\theta - \theta_l)/\Delta\theta,$$

$$S = (C - C_l)/\Delta C, \quad Pr = \nu/\kappa, \quad Le = \kappa/D, \quad Ar = H/L,$$

$$R_t = g\beta_t \Delta\theta L^3/\kappa\nu, \quad R_s = g\beta_s \Delta C L^3/\kappa\nu, \quad R_\rho = (\beta_s \Delta C)/(\beta_t \Delta\theta) = R_s/R_t.$$

As is evident in the foregoing formulations, the relevant fluid properties are: kinematic viscosity, $\nu$; thermal diffusivity, $\kappa$; solutal diffusivity, $D$; and coefficient of volumetric expansion with temperature (solute), $\beta_t(\beta_s)$. The relevant non-dimensional parameters are: the Prandtl number, $Pr$; the Lewis number, $Le$; the thermal Rayleigh number, $R_t$; the solutal Rayleigh number, $R_s$; and the cavity aspect ratio, $Ar$.

A schematic of the flow configuration is shown in Fig. 1. The cavity is of width $L$ and height $H$, and the Cartesian coordinates $(x, y)$, with the corresponding velocity components $(u, v)$, are indicated therein. As ascertained earlier, in the initial state, the fluid is motionless and at uniform temperature ($T = 0$). However, the fluid has already been stably stratified by a vertically-linear distribution of solute. At the initial instant $t = 0$, the temperature of the left vertical sidewall ($X = 0$) is abruptly raised to $T = 1$ and is maintained thereafter. All the boundary walls of the cavity are impermeable to solute, i.e. $\partial S/\partial n = 0$. The ensuing

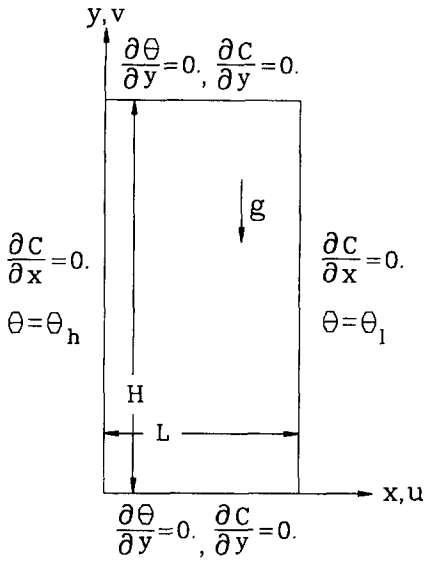


FIG. 1. Flow configuration and coordinate system.

motions inside the cavity are to be studied. Hence, the proper initial and boundary conditions are

$$U = V = T = 0, \quad S = 1 - Y/Ar \text{ at } \tau = 0;$$

$$U = V = \frac{\partial S}{\partial n} = 0 \text{ on all solid boundaries;}$$

$$T = 1 \text{ on } X = 0, \quad T = 0 \text{ on } X = 1;$$

$$\frac{\partial T}{\partial Y} = 0 \text{ on } Y = 0, \quad Ar.$$

In the actual computations, the Prandtl number $Pr$ and the Lewis number $Le$ were set to 7.0 and 100.0, respectively, to simulate the approximate values of salt water. The aspect ratio $Ar$ and the thermal Rayleigh number $R_t$ were fixed at 2.0 and $10^7$, respectively. The solutal Rayleigh number $R_s$, and, accordingly, the buoyancy ratio $R_\rho$, were the major variable parameters. In the present calculations, in an effort to examine the flow behaviour in both the supercritical and subcritical regimes, $R_\rho$ covers a wide range 0.0–50.0. Obviously, $R_\rho = 0.0$ corresponds to the case of purely thermal convection.

The numerical techniques to solve the above equations have been well established. We have chosen an amended version of the SIMPLER algorithm, which was originally developed by Patankar [18]. The SIMPLER algorithm is based on an iterative method, and the convergence criteria are needed. In the present study, we have adopted the following convergence criteria at each time step:

$$\frac{\left|\left(\frac{\partial U}{\partial X} + \frac{\partial V}{\partial Y}\right)_{i,j}\right|_{\max}}{|U_{i,j}|_{\max}} < \varepsilon_1, \quad \left|\frac{\phi_{i,j}^{k+1} - \phi_{i,j}^{k}}{\phi_{i,j}^{k+1}}\right|_{\max} < \varepsilon_2$$

where $\varepsilon_1$ and $\varepsilon_2$ are typically $10^{-6}$ and $10^{-4}$, respectively, $\phi$ indicates the physical variable of interest, and superscript $k$ denotes the iteration index. The grid net was highly stretched in the vicinity of the solid walls to improve resolution of the boundary layers. The typical grid points in the present study were $(51 \times 85)$, and appropriate modifications were made to the mesh when finer mesh nets were desired.

Mention should be made of the parallel numerical computations [19, 20], which have tackled double diffusive convection in a rectangle when the horizontal gradients, of both the temperature and solute, are concurrently imposed on the vertical sidewalls. The specifics of the numerical models employed in these studies were the same as the present work. The above studies have clearly illustrated the agreement between the numerical results and the available experimental observations [21, 22]. This close agreement documented in the above reports gives credence to the soundness of the numerical techniques being utilized in the present numerical computations.

## 3. RESULTS AND DISCUSSION

The results of extensive numerical computations will be organized so as to clearly portray the principal flow characteristics in the two regimes as classified by Chen *et al.* [14], i.e. the supercritical ($Ra > 1.5 \times 10^4$) and subcritical ($Ra < 1.5 \times 10^4$) regimes. Here, the Rayleigh number is defined by using the length scale $\eta\,(\equiv \rho_r \beta_t \Delta\theta / |(\mathrm{d}\rho/\mathrm{d}y)|_0) = H/R_\rho$ as the reference length scale. Therefore, $Ra\,(\equiv g\beta_t \Delta\theta \eta^3/\kappa\nu) = R_t(Ar/R_\rho)^3$, and it follows that, for a given set of parameter values, $Ra$ is determined when the value of $R_\rho$ is assigned.

Before proceeding to detailed analyses of the main results, we shall scrutinize the gross features of the flow in the very early phases. As expected, the early-time behaviour displays substantial qualitative similarities between the two regimes. Figure 2 shows the

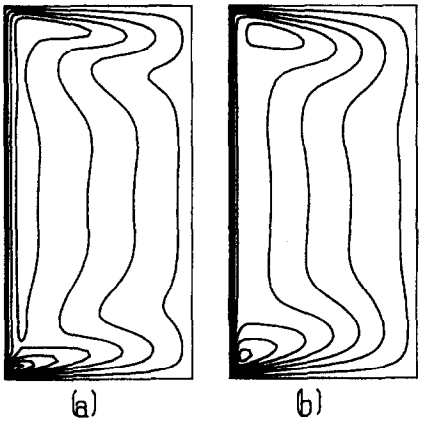


FIG. 2. Plots of stream functions at an early time ($\tau = 0.0005$). Conditions are (a) $Ra = 10^4$ ($R_\rho = 20.0$) and (b) $Ra = 2.33 \times 10^5$ ($R_\rho = 7.0$). Maximum and minimum values of $\psi$ are (a) $\psi_{\max} = 0$, $\psi_{\min} = -0.5298 \times 10$; (b) $\psi_{\max} = 0$, $\psi_{\min} = -0.1365 \times 10^2$. Values for $\psi$ are, from the boundary to the interior, $0.05\psi_{\min}$, $0.20\psi_{\min}$, $0.35\psi_{\min}$, $0.50\psi_{\min}$, $0.65\psi_{\min}$, $0.80\psi_{\min}$ and $0.95\psi_{\min}$.

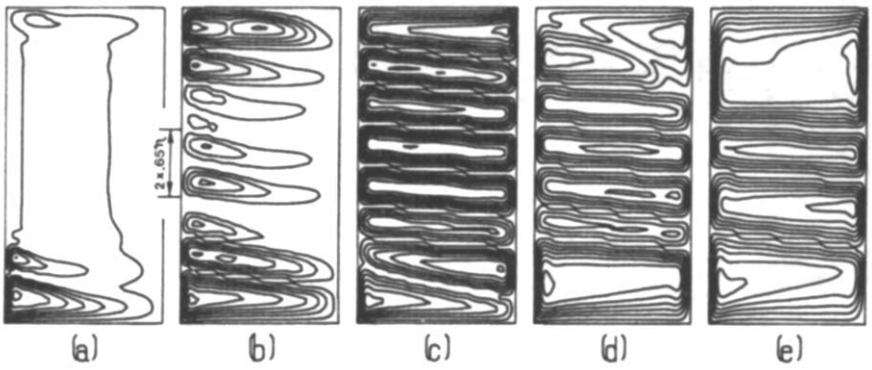


FIG. 3. Time evolving plots of stream functions for $Ra = 2.33 \times 10^5$ ($R_\rho = 7.0$). Times are: (a) $\tau = 0.005$; (b) $\tau = 0.02$; (c) $\tau = 0.05$; (d) $\tau = 0.09$; (e) $\tau = 0.30$. Values for $\psi$ are the same as in Fig. 2. (a) $\psi_{min} = -0.1572 \times 10^2$, $\psi_{max} = 0.1264$; (b) $\psi_{min} = -0.1959 \times 10^2$, $\psi_{max} = 0.1664 \times 10$; (c) $\psi_{min} = -0.1845 \times 10^2$, $\psi_{max} = 0.4259 \times 10^{-5}$; (d) $\psi_{min} = -0.1634 \times 10^2$, $\psi_{max} = 0.1062$; (e) $\psi_{min} = -0.3196 \times 10^2$, $\psi_{max} = 0.1212$.

numerically-constructed stream patterns at a very early time ($\tau = 0.0005$), by plotting contours of the stream function $\psi$. As is customary practice, $\psi$ is defined such that $U = \partial\psi/\partial Y$, $V = -\partial\psi/\partial X$. Along the left vertical wall, almost-parallel vertically-upward motions are induced by the impulsively-applied thermal forcing at the boundary. In both regimes, the first appearance of cell(s) is noticeable in the corner region(s) near the heated vertical wall. These depictions of the early time behaviour are qualitatively consistent with the previous observations (see, e.g. Thorpe *et al.* [7] and Wirtz *et al.* [17]).

First, we shall focus attention on the results in the supercritical regime. Figures 3–5 present the numerical results which depict the evolution of flow (Fig. 3), thermal (Fig. 4) and solutal (Fig. 5) fields for an illustrative case in this regime ($R_\rho = 7.0$, thus $Ra = 2.33 \times 10^5$). The left vertical sidewall is being heated, therefore, as shown in Fig. 3, the sense of rotation of the major cells is clockwise. However, a closer inspection of the flow data points to the presence of secondary cells in the interfaces of layers and/or in the near-stagnant regions. The sense of rotation in these secondary cells is counter-clockwise. Nevertheless, it should be remarked that the strengths of the secondary cells are substantially lower than those of the major cells. Therefore, in the figures, the presence of secondary cells is not clearly captured since the magnitudes are very small (compare the maximum and minimum values of $\psi$ in Fig. 3).

We shall now describe in more detail the characteristic behaviour in several temporal stages. In the early phase (see, e.g. the results for $\tau = 0.005$), the horizontal layers are visible only near the bottom horizontal wall. This region corresponds to the area where the temperature field shows instability. With the exception of this near-bottom wall region, the isotherms are fairly parallel to the heated sidewall. This indicates the dominance of the conductive heat transfer mode in the vicinity of the heated wall. The concentration field is also quite revealing. In the region near the heated sidewall, the horizontal density gradient forced by the lateral heating tends to be mitigated by the transport of fluid of higher concentration from the lower level. The concentration at the far field away from the heated sidewall still maintains the original vertically-linear distribution.

As time progresses (see the results for $\tau = 0.02$), the

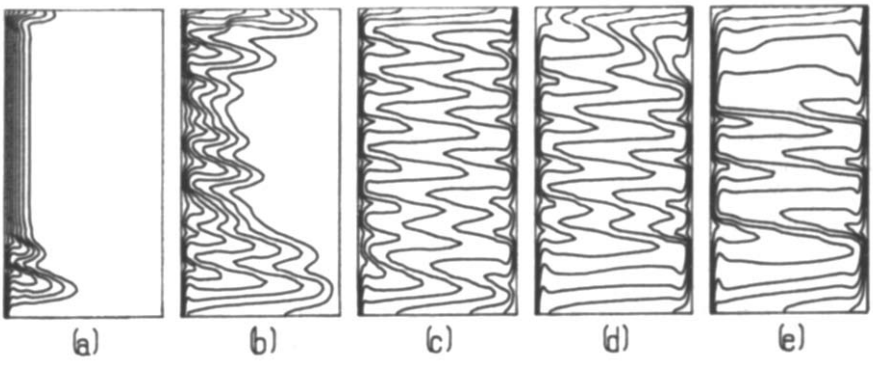


FIG. 4. Time evolving plots of isotherms for $Ra = 2.33 \times 10^5$ ($R_\rho = 7.0$). Times are the same as in Fig. 3. Values for isotherms are, from left to right, 0.875, 0.750, 0.625, 0.500, 0.375, 0.250 and 0.125.

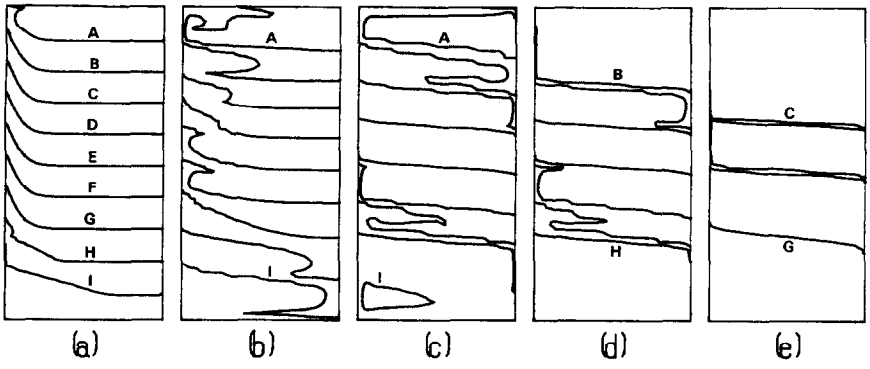


FIG. 5. Time evolving plots of iso-concentration lines for $Ra = 2.33 \times 10^5$ ($R_\rho = 7.0$). Times are the same as in Fig. 3. Values for iso-concentration lines are: A, 0.1; B, 0.2; C, 0.3; D, 0.4; E, 0.5; F, 0.6; G, 0.7; H, 0.8; I, 0.9. Maximum and minimum values of concentration are: (a) $S_{min} = 0.3850 \times 10^{-2}$, $S_{max} = 0.9954$; (b) $S_{min} = 0.6893 \times 10^{-2}$, $S_{max} = 0.9673$; (c) $S_{min} = 0.8532 \times 10^{-1}$, $S_{max} = 0.9060$; (d) $S_{min} = 0.1102$, $S_{max} = 0.8512$; (e) $S_{min} = 0.2362$, $S_{max} = 0.7773$.

influence of the heated sidewall has advanced further into the interior. The temperature field discloses unstable configurations in wider portions of the cavity. This is concomitant with the production of more of the horizontally propagating rolls in the bulk of the flow field. The heated fluid element ceases upward motion at the level where the original density distribution compensates the density deficit caused by the lateral heating. Once this level is reached, the fluid element turns in the horizontal direction, thereby a layered structure is formed. The fluid that moves away from the heated sidewall shows a slightly downward tilt, since it loses heat to the cold ambient fluid on this excursion [15]. As demonstrated in Fig. 3(b), the height of the layer $h$, when scaled by $\eta\,(\equiv H/R_\rho)$, is found to be compatible with the estimate of Huppert and Turner [15], i.e. $h/\eta \cong 0.62$. The concentration field, in association with the layered velocity field, shows appreciable mixing within each layer owing to vigorous convective activities.

At a still later time (see the results for $\tau = 0.05$), the rolls seem to have reached the opposite cold sidewall. The entire cavity is filled with fully-developed layers, and these layers are separated by very thin interfaces. Since the thermal diffusivity is much larger than the solutal diffusivity, the thermal adjustment is more rapid, and therefore, the thermal field readily conforms to the layered velocity structure. The thermal field is stably stratified within each layer. This computed thermal field is consistent with the experimental observations of Thorpe *et al.* [7]. After this stage, the merging process takes place, i.e. two adjacent layers merge into a new, single layer. This was also seen in the experiments of Wirtz and Reddy [23]. The temperature and concentration fields are adjusted accordingly. The merging process persists to a rather large time. The plots shown for the largest time instant computed in the present study ($\tau = 0.3$) exhibit the general trend of the flow approaching the steady state. All the rigid boundary walls of the cavity are impermeable for salinity; as the merging process continues, the concentration field tends to be equalized in the whole cavity, due mainly to convective mixing and partly to the diffusion of solute. This implies that, encompassing the various stages of transition, the pre-existing linear solute distribution in the initial stage is being destroyed. This is the expected consequence of the pre-set conditions that there are no sources or sinks of the solute on the boundaries of the cavity. The final state will therefore be characterized by a unicell flow pattern and stably-stratified thermal field, together with a homogeneous concentration ($S = 0.5$).

The time evolutions pictured here are qualitatively similar to the prior results of Wirtz *et al.* [17] at $Ra = 10^5$. The present study, being more specific and comprehensive, has clearly demonstrated the explicit and detailed flow patterns of the horizontally propagating cells and the associated thermal and solute fields.

As stated carlier, one of the striking features that were uncovered by the previous experiments was the existence of the distinctly-defined layered structure. In the present study, such a layered structure has been convincingly ascertained by extensive numerical results. In order to gain further physical insight, Fig. 6 exhibits the vertical profiles of the local Nusselt number $Nu\,(\equiv -\partial T/\partial X|_{X=0})$ at the heated sidewall, and of temperature and concentration along the mid-width ($X = 0.5$) at time instant $\tau = 0.05$. Note that, in these intermediate stages, the whole cavity is filled with well-organized horizontal layers (see Fig. 3(c)). Careful inspection of the $Nu$ profile of Fig. 6 indicates that the local maxima correspond to the levels of the centres of the layers (exactly speaking, to the slightly lower part of the centres of the layers due to clockwise circulation), and the local minima to those of the interfaces between the layers. This spatially periodic behaviour of the vertical profile of $Nu$ is in close agreement with the experimental findings of Huppert and Turner [15]. As in the foregoing statements, the temperature field is stably stratified in the localized

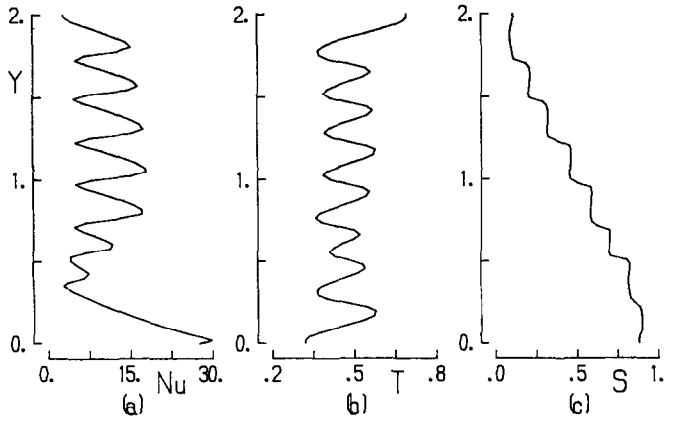


FIG. 6. Vertical profiles of (a) the local $Nu$ at $X = 0$, (b) temperature and (c) concentration at $X = 0.5$. Conditions are $Ra = 2.33 \times 10^5$ ($R_\rho = 7.0$) and $\tau = 0.05$.

area within the layer, and the conductive mode is prevailing in the regions of the interfaces. The characteristic S-shaped temperature profile bears this point. The salinity profile displays a step-like distribution. Within each layer, concentration is substantially uniform due principally to convective mixing. The above numerical results are in fair agreement with the prior experimental observations (see, e.g. Thorpe *et al.* [7] and Huppert and Turner [15]). Such consistency is highly encouraging; the specific comparisons between the present numerical simulations and the preceding experiments are mutually-supportive of each other. In particular, the present numerical data are strongly corroborative of the experiments both in qualitative observations and quantitative measurements. In passing, a further scrutiny of the temperature and concentration profiles of Fig. 6 reveals that the interfaces are of the diffusive type; i.e. the fluid of high temperature and high concentration underlies the fluid of low temperature and low concentration [9].

As part of an effort to adduce the time-dependent layered flow structure, the vertical profiles of the horizontal velocity along mid-width ($X = 0.5$) are plotted in Fig. 7. Three different time instants are represented to portray the evolutions. At an early time ($\tau = 0.005$), the broad stagnant region occupying much of the interior is discernible. As illustrated in Figs. 3(b)–(d), highly fluctuating velocity profiles are visible at intermediate and large times, reflecting the presence of the layered structure. As time elapses, the overall solute gradient, which was initially strongly stabilizing, weakens as a consequence of convective mixing. After the process of layer-merging commences, the convective activity is, in general, enhanced. This may be explained by noting that the effective Rayleigh number of a merged layer is larger than the Rayleigh number of an individual component layer before the merging. It should also be mentioned that, by way of the merging process, the heights of the layers undergo readjustments, as is apparent in the plots of the stream function $\psi$ in Fig. 3.

In order to assess the effect of $Ra$ on the trend of flow characteristics, several more runs have been computed. Figure 8, at $Ra = 8 \times 10^4$ ($R_\rho = 10.0$), displays the flow evolutions toward the establishment of the fully-layered structure in the whole cavity. The value of $Ra$ in Fig. 8 is smaller than that shown in Fig. 3, but this still belongs to the supercritical regime

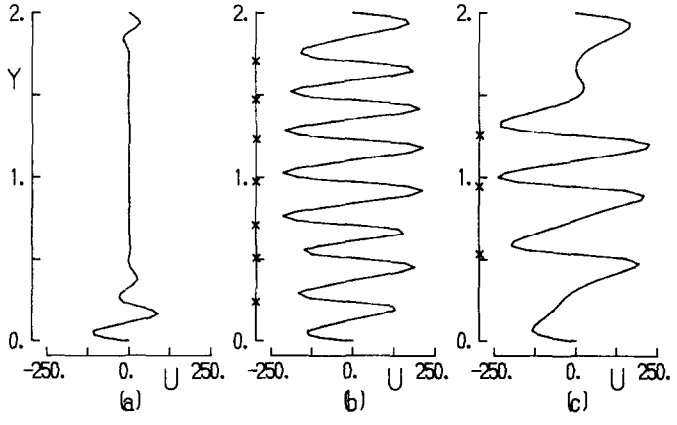


FIG. 7. Vertical profiles of horizontal velocity at $X = 0.5$. Conditions are $Ra = 2.33 \times 10^5$ ($R_\rho = 7.0$). Times are: (a) $\tau = 0.005$, (b) $\tau = 0.05$ and (c) $\tau = 0.3$. The locations of interfaces at mid-width ($X = 0.5$) are denoted by $\times$.

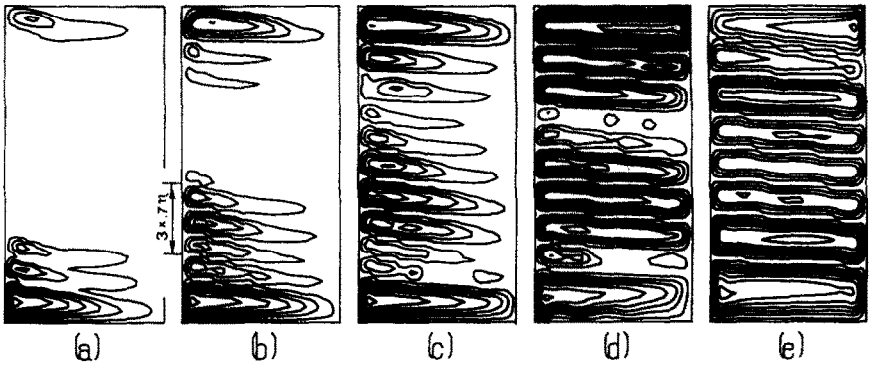


FIG. 8. Time evolving plots of stream functions for $Ra = 8 \times 10^4$ ($R_\rho = 10.0$). Times are: (a) $\tau = 0.01$, (b) $\tau = 0.02$, (c) $\tau = 0.03$, (d) $\tau = 0.05$, (e) $\tau = 0.10$. Values for $\psi$ are the same as in Fig. 2. (a) $\psi_{min} = -0.1498 \times 10^2$, $\psi_{max} = 0.4850$; (b) $\psi_{min} = -0.1611 \times 10^2$, $\psi_{max} = 0.1079 \times 10$; (c) $\psi_{min} = -0.1626 \times 10^2$, $\psi_{max} = 0.1638 \times 10$; (d) $\psi_{min} = -0.1714 \times 10^2$, $\psi_{max} = 0.9333$; (e) $\psi_{min} = -0.2484 \times 10^2$, $\psi_{max} = 0.1427$.

as classified by Chen *et al.* [14]. At small times (Fig. 8(a) for $\tau = 0.01$ and Fig. 8(b) for $\tau = 0.02$), several rolls are formed in the vicinity of the horizontal walls. However, a part of the interior surrounding the mid-depth is still substantially motionless, constrained by the prevailing stable concentration gradient. The height $h$ of the layer is found to be comparable to the predictions by Huppert and Turner [15], i.e. $h/\eta \cong 0.62$. The subsequent plots exhibited in Figs. 8(c), (d) and (e) demonstrate the gradual increase of the number of layers and the horizontal propagation of these layers. Figure 8(e), at a relatively large time $\tau = 0.1$, shows a plot which depicts the stage when the whole cavity is filled with a system of well-developed horizontal layers. In the transition process of reaching this stage, several cells of smaller sizes and of substantially diminished magnitudes rapidly merge and/or disappear.

Figure 9 shows the results at a higher $Ra$ ($Ra = 2.96 \times 10^6$, $R_\rho = 3.0$) than that in Fig. 3. At this high $Ra$, the way the layers are formed near the heated sidewall is more simultaneous than were seen at lower Rayleigh numbers. These spontaneously-formed layers propagate toward the opposite wall more rapidly than the cases of lower Rayleigh numbers. The scale of layer height $h$ is still compatible with the predictions of Huppert and Turner [15], i.e. $h/\eta \cong 0.62$. As is intuitively clear, a higher $Ra$ implies, in the present study, a lower $R_\rho$; accordingly, the comparative magnitudes of the convective activities in the transition phases are stronger, since the prevailing solutal effects are weaker. Both the generation of layers and subsequent merging of the adjacent layers proceed more vigorously at higher Rayleigh numbers. At the relatively large time instant shown in Fig. 9(e) for $\tau = 0.1$, only two distinct layers are discernible. For this particular run, calculations were performed to a very large time, $\tau = 0.6$. Flows evolve very slowly at such large times, but the results confirm the expectations. At $\tau = 0.6$ (Fig. 8(f)), the unicell flow patterns are obtained. This is very akin to the well-known steady-state flow field in a purely thermal convection at high Rayleigh numbers in a cavity with differentially heated sidewalls [24]. This can easily be anticipated in view of the fact that there are no reservoirs for solute in the present problem.

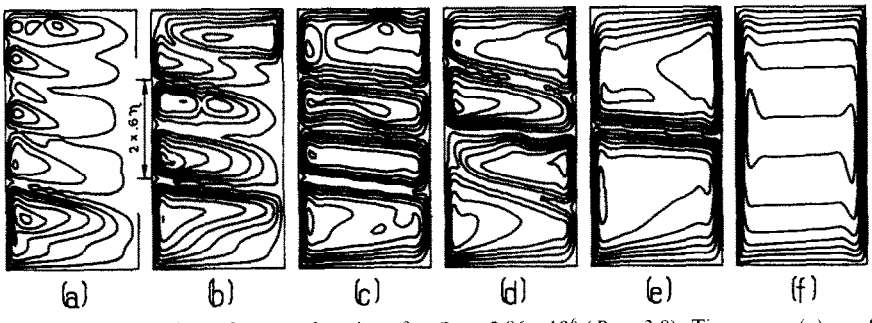


FIG. 9. Time evolving plots of stream functions for $Ra = 2.96 \times 10^6$ ($R_\rho = 3.0$). Times are: (a) $\tau = 0.01$, (b) $\tau = 0.02$, (c) $\tau = 0.03$, (d) $\tau = 0.05$, (e) $\tau = 0.10$, (f) $\tau = 0.60$. Values for $\psi$ are the same as in Fig. 2. (a) $\psi_{min} = -0.3336 \times 10^2$, $\psi_{max} = 0.5037$, (b) $\psi_{min} = -0.3265 \times 10^2$, $\psi_{max} = 0.9985$; (c) $\psi_{min} = -0.3718 \times 10^2$, $\psi_{max} = 0.4419$; (d) $\psi_{min} = -0.3027 \times 10^2$, $\psi_{max} = 0.1002 \times 10$; (e) $\psi_{min} = -0.3794 \times 10^2$, $\psi_{max} = 0.0$; (f) $\psi_{min} = -0.5908 \times 10^2$, $\psi_{max} = 0.0$.

Now, we shall turn to the subcritical regime ($Ra < 1.5 \times 10^4$) as categorized by Chen *et al.* [14]. It has previously been asserted that, in the subcritical regime, the layers form successively rather than simultaneously as was seen in the supercritical regime. The numerical results for a representative subcritical condition ($Ra = 10^4$, $R_\rho = 20.0$) are illuminated in Figs. 10–12. At small times (see Figs. 10(a), 11(a) and 12(a) for $\tau = 0.01$), the convective activities are restricted to a narrow region very close to the bottom wall. The prevailing solute gradient is substantial so that convective motions are accordingly less vigorous. Over much of the length of the heated sidewall, the isotherms are parallel, implying that the dominant heat transfer mode is conduction. Only in the bottom corner area do the isotherm patterns suggest weak

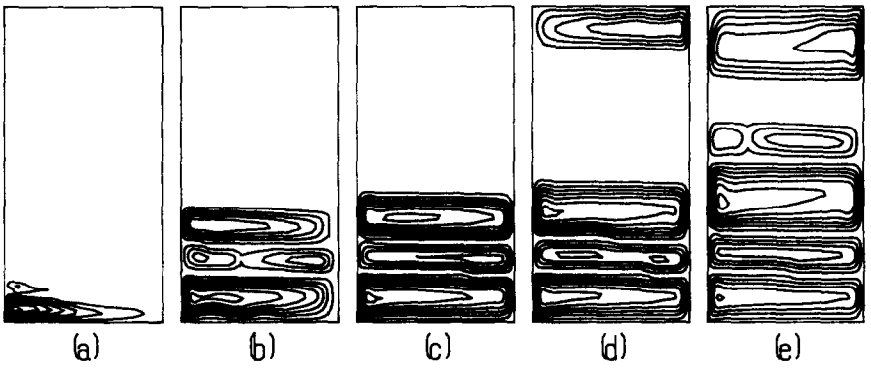


FIG. 10. Time evolving plots of stream functions for $Ra = 10^4$ ($R_\rho = 20.0$). Times are: (a) $\tau = 0.01$, (b) $\tau = 0.10$, (c) $\tau = 0.20$, (d) $\tau = 0.30$, (e) $\tau = 0.50$. Values for $\psi$ are the same as in Fig. 2. (a) $\psi_{min} = -0.9444 \times 10$, $\psi_{max} = 0.2965$; (b) $\psi_{min} = -0.1766 \times 10^2$, $\psi_{max} = 0.7225$; (c) $\psi_{min} = -0.2035 \times 10^2$, $\psi_{max} = 0.6824$; (d) $\psi_{min} = -0.2317 \times 10^2$, $\psi_{max} = 0.4990$; (e) $\psi_{min} = -0.3103 \times 10^2$, $\psi_{max} = 0.6702$.

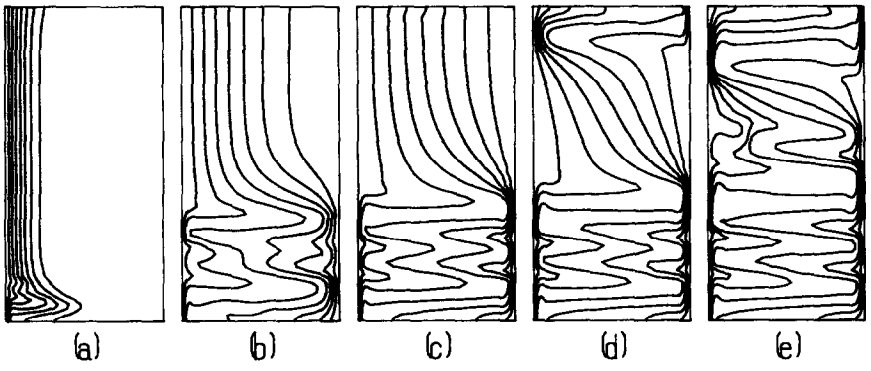


FIG. 11. Time evolving plots of isotherms for $Ra = 10^4$ ($R_\rho = 20.0$). Times are the same as in Fig. 10. Values for the isotherms are the same as in Fig. 4.

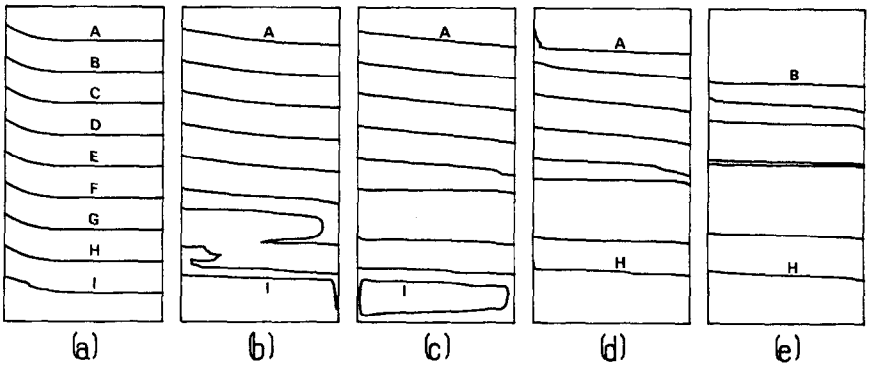


FIG. 12. Time evolving plots of iso-concentration lines for $Ra = 10^4$ ($R_\rho = 20.0$). Times are the same as in Fig. 10. Values for the iso-concentration lines are the same as in Fig. 5. (a) $S_{min} = 0.5164 \times 10^{-2}$, $S_{max} = 0.9928$; (b) $S_{min} = 0.1127 \times 10^{-1}$, $S_{max} = 0.9280$; (c) $S_{min} = 0.1336 \times 10^{-1}$, $S_{max} = 0.9053$; (d) $S_{min} = 0.6909 \times 10^{-1}$, $S_{max} = 0.8860$; (e) $S_{min} = 0.1198$, $S_{max} = 0.8509$.

convective motions. Similarly, the pre-existing vertically-linear solutal field remains virtually unaffected in the bulk of the cavity. Only very near the heated sidewall, in particular, in the bottom corner region, is a slight upward tilting of the iso-solutal contours seen. At later times, the sequential plots for $\tau = 0.10$ and 0.20 clearly demonstrate the successive appearance of a new layer on top of the layers already in existence. In conjunction with the successive generation of the layers, the upper regions of vertically parallel isotherms, where conduction is dominant, shrink in size in the vertical extent toward the top wall. However, the conduction-dominant thermal field advances toward the cold vertical sidewall. In the bottom portions of the cavity, thermal instability is induced, which brings about the successive formation of layers. Over these intermediate transition stages, the layer height $h$ is not scaled with $O(\eta)$. As shown in Figs. 10(b)–(d), in the intermediate phases, as time elapses, the overall strengths of convective motions increase; also, the height of the top-most layer of the system of layers in the lower regions of the cavity increases. On the other hand, the thicknesses of the two bottom layers remain fairly constant after $\tau \sim 0.1$; the growth of these two bottom layers is constrained by the bottom boundary wall and the top-most layer near the central portion of the cavity. At a relatively large time (see Fig. 10(d) for $\tau = 0.30$), a layer forms near the top boundary wall. The corresponding features also take place near the top wall in the temperature and solutal fields. As ascertained previously, the formation of layers is accompanied by stable temperature fields and well-mixed solute distributions in the localized regions concerned. A perusal of the numerical results reveals that the appearance of the layer near the top wall is delayed to a later time as $Ra$ decreases, i.e. as $R_\rho$ increases. This is attributable to the influence of a stronger pre-existing stabilizing solute distribution, which inhibits thermal convection in the cavity. As time progresses further, at a very large time (see Fig. 10(e) for $\tau = 0.5$), a new layer is formed above the upper-most layer of the system of layers in the lower regions of the cavity. It is worth noting that the adjustment of the solutal field toward complete homogenization takes place at a slow rate. It is obvious that the large-time evolution is accomplished at a much slower rate in the subcritical regime than in the supercritical regime.

By the preceding comparisons of the numerical results, which are typical of the supercritical (see Figs. 3–5) and the subcritical regime (see Figs. 10–12), it is now clear that the evolutionary processes of layer formations can be characterized as being simultaneous and successive in these two regimes, respectively.

In order to further the details of the characteristics of the subcritical regime, using the results of Figs. 10–12, the local Nusselt number at the left vertical wall, the temperature and solute profiles along the mid-width ($X = 0.5$) at a relatively large time ($\tau = 0.20$) are plotted in Fig. 13. In a manner similar to the case of the supercritical regime, the $Nu$ profile contains local maxima at the centres of the layers and local minima at the interfaces. Also, the S-shaped temperature profile and the step-like solutal distribution are manifested in the region occupied by the layers. However, as stated earlier, the layer formation is successive; therefore, in the upper portions of the cavity where no layers have been formed, $Nu = O(1)$. This reflects the fact that convection is suppressed and the heat transfer is mainly effectuated by conduction in this region. The temperature decreases monotonically vertically upward, and the solutal distribution maintains the original linear gradient. Only in a narrow area adjacent to the top wall are a slight stratification of the thermal profile and a locally homogenized solutal field visible; this implies the initiation of the layer near the top wall as displayed in Fig. 10(e) at this time instant.

The above examinations of the comprehensive numerical data are supportive of the characterizations offered by Chen *et al.* [14] with regard to the existence of the critical Rayleigh number $Ra_c \cong 1.5 \times 10^4$. In an effort to validate the quantitative soundness of this estimate of $Ra_c$, several more runs have been executed using values of $Ra$ in the close neighbourhood of the experimentally observed value of $Ra_c \cong 1.5 \times 10^4$.

Figure 14 shows the flow evolutions at $Ra = 2.37 \times 10^4$ ($R_\rho = 15.0$), a value slightly higher than $Ra_c$. As depicted in Fig. 14(b), at a reasonably small time ($\tau = 0.03$), several layers are formed in the bottom region, which is similar to the preceding results in Fig. 10. However, it is noticeable that a layer appears near the top wall even in this early phase. It is also worth pointing out that the height of the layer, $h/\eta$, assumes a value slightly less than unity. This is strongly consistent with the prior observations by Chen *et al.* [14] and Huppert and Turner [15]. These previous accounts asserted that $h/\eta$ falls steadily from unity to a value of $0.62 \pm 0.05$ as $Ra$ increases from $Ra_c$ to a value of around $5 \times 10^5$. In summary, the results at a value of $Ra$ near the borderline of $Ra_c$, show a hybrid nature exhibiting the character of both the supercritical and subcritical regimes. For the run of Fig. 14, the appearance of the layer near the top wall in the early stage weighs more heavily toward a characterization of the simultaneous, rather than successive, flow evolution of the supercritical regime.

In contrast to the results of Fig. 14, Fig. 15 portrays the flow patterns at $Ra = 2.96 \times 10^3$ ($R_\rho = 30$), a value slightly lower than that shown in Figs. 10–12. During the entire transient phase up to a very large time ($\tau = 0.51$), only a single layer, formed near the bottom wall, is discernible. As time progresses, this single layer grows in size, indicating the increase of convective activity in this region. In the bulk of the flow field, the convective motions are inhibited by the strong influence of the pre-existing stable concentration gradient. Similar results were obtained from other runs, using values of $Ra$ further below $Ra_c$.

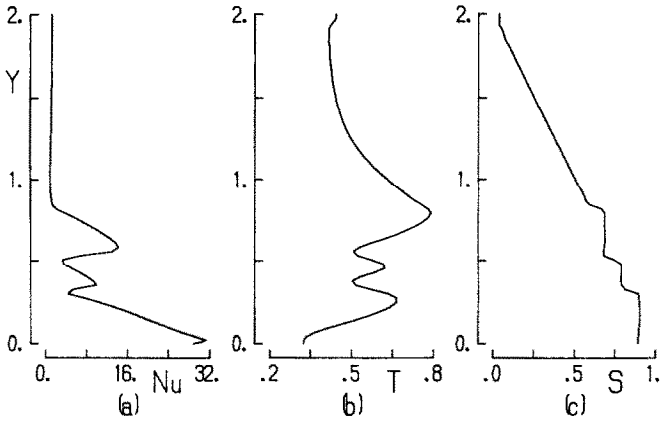


FIG. 13. Vertical profiles of (a) the local $Nu$ at $X = 0$, (b) temperature and (c) concentration at $X = 0.5$. Conditions are $Ra = 10^4$ ($R_\rho = 20.0$) and $\tau = 0.20$.

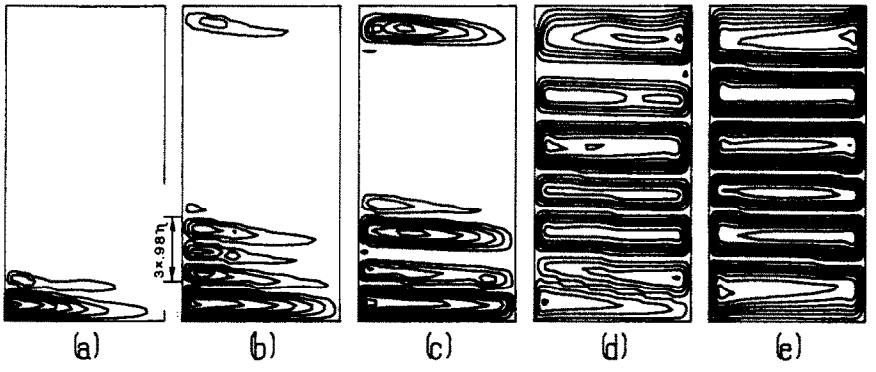


FIG. 14. Time evolving plots of stream functions for $Ra = 2.37 \times 10^4$ ($R_\rho = 15.0$). Times are: (a) $\tau = 0.01$, (b) $\tau = 0.03$, (c) $\tau = 0.05$, (d) $\tau = 0.15$, (e) $\tau = 0.30$. Values for $\psi$ are the same as in Fig. 2. (a) $\psi_{min} = -0.1180 \times 10^2$, $\psi_{max} = 0.4871$; (b) $\psi_{min} = -0.1358 \times 10^2$, $\psi_{max} = 0.8357$; (c) $\psi_{min} = -0.1439 \times 10^2$, $\psi_{max} = 0.1372 \times 10$; (d) $\psi_{min} = -0.2697 \times 10^2$, $\psi_{max} = 0.1348 \times 10$; (e) $\psi_{min} = -0.2489 \times 10^2$, $\psi_{max} = 0.1460$.

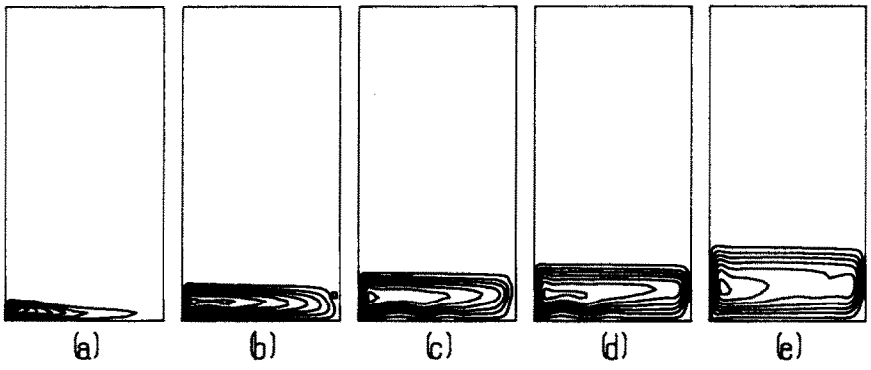


FIG. 15. Time evolving plots of stream functions for $Ra = 2.96 \times 10^3$ ($R_\rho = 30.0$). Times are: (a) $\tau = 0.01$, (b) $\tau = 0.10$, (c) $\tau = 0.20$, (d) $\tau = 0.30$, (e) $\tau = 0.51$. Values for $\psi$ are the same as in Fig. 2. (a) $\psi_{min} = -0.6646 \times 10$, $\psi_{max} = 0.5895$; (b) $\psi_{min} = -0.1376 \times 10^2$, $\psi_{max} = 0.5225$; (c) $\psi_{min} = -0.1802 \times 10^2$, $\psi_{max} = 0.5949$; (d) $\psi_{min} = -0.1970 \times 10^2$, $\psi_{max} = 0.1761$; (e) $\psi_{min} = -0.2966 \times 10^2$, $\psi_{max} = 0.4660$.

Figure 16 is designed to illustrate the explicit effect of $Ra$ on the local Nusselt number at the heated sidewall. Figure 16(a) typifies the results at a small time ($\tau = 0.01$). The maximum value of $Nu$, in general, increases as $Ra$ increases. This is anticipated since, at high $Ra$, the bottom layer is developed at an earlier time instant and intensifies more rapidly. At a very small value of $Ra$, much of the heat transfer near the heated sidewall is conduction dominant. The fluctuating $Nu$ profile at large $Ra$ is clearly in line with the

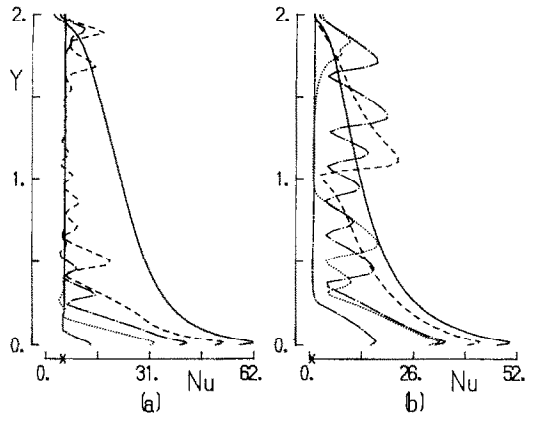


FIG. 16. Vertical profiles of the local $Nu$ at $X = 0$. Times are (a) $\tau = 0.01$ and (b) $\tau = 0.3$. The values of $Ra$ are: ———, $Ra = 8 \times 10^3$ ($R_p = 0.0$, purely thermal convection); - - - -, $Ra = 6.4 \times 10^5$ ($R_p = 5.0$); — · — · —, $Ra = 8 \times 10^4$ ($R_p = 10.0$); · · · ·, $Ra = 10^4$ ($R_p = 20.0$); — · · — · · —, $Ra = 6.40 \times 10^2$ ($R_p = 50.0$). The location of symbol × on the abscissa denotes the value of $Nu$ obtainable under conduction.

initiation of the roll formation near the heated sidewall. Figure 16(b) shows the results at a large time ($\tau = 0.3$). At large $Ra$, the conduction-controlled heat transfer virtually disappears, and the fluctuating $Nu$ profile, compatible with the layered flow structure, is in evidence. The maximum convective heat transfer takes place in the regions occupied by the bottommost layer.

## 4. CONCLUSION

Comprehensive and thorough analyses have been made of the numerical solutions for the time-dependent double diffusive convection in a cavity. The numerical results showed that the fundamental character of the flow may be classified into the supercritical ($Ra > Ra_c \cong 1.5 \times 10^4$) and subcritical ($Ra < Ra_c$) regimes. This categorization is consistent with the prior observations by Chen *et al.*

In the supercritical regime, the appearance of the horizontal layers, formed in the heated sidewall and subsequently propagating horizontally toward the cold sidewall, takes place simultaneously along the heated sidewall except in the vicinity of horizontal walls. The characteristic S-shaped temperature profile and the step-like solute distribution are visible in the whole cavity, in line with the establishment of the layered flow structure.

In the subcritical regime, the formation of the horizontal layers is achieved successively, commencing at the bottom wall and new layers are sequentially formed above the top of the already-developed layers. In the regions where no layers have yet formed, the temperature field is conduction dominant and the solutal field retains the original pre-existing vertically-linear gradient. The descriptions obtainable from the numerical solutions of the gross features of the evolutions of the flow fields are in close qualitative agreement with the available experimental visualizations. The height of the layer $h$ was found to be scaled with $\eta$; this finding is in support of the contentions derived by the previous estimates by Huppert and Turner.

The quantitative reasonableness of the value of $Ra_c \cong 1.5 \times 10^4$, given by Chen *et al.*, has been tested by the present numerical results. Careful comparisons of the computed data reveal that the value of $Ra_c$ based on the experimental finding satisfactorily indicates the demarcation line separating the subcritical and supercritical regime.

## REFERENCES

1. J. S. Turner, Double diffusive phenomena, *Ann. Rev. Fluid Mech.* **6**, 37–56 (1974).
2. J. S. Turner, Multi-component convection, *Ann. Rev. Fluid Mech.* **17**, 11–44 (1985).
3. H. E. Huppert and J. S. Turner, Double diffusive convection, *J. Fluid Mech.* **106**, 299–329 (1981).
4. J. S. Turner, The behavior of a stable salinity gradient heated from below, *J. Fluid Mech.* **33**, 183–200 (1968).
5. F. P. Incropera and R. Viskanta, Optical studies of mixed layer development in a double diffusive, thermohaline convection, *Proc. 7th Int. Heat Transfer Conf.*, Vol. 2, pp. 419–424 (1982).
6. S. Ostrach, Natural convection with combined driving forces, *PhysicoChem. Hydrodyn.* **1**, 233–247 (1980).
7. S. A. Thorpe, P. K. Hutt and R. Soulsby, The effect of horizontal gradients on thermohaline convection, *J. Fluid Mech.* **38**, 375–400 (1969).
8. Y. Suzukawa and U. Narusawa, Structure of double-diffusive convection cells, *J. Heat Transfer* **104**, 248–254 (1982).
9. J. Tanny and A. B. Tsinober, The dynamics and structure of double-diffusive layers in sidewall-heating experiments, *J. Fluid Mech.* **196**, 135–156 (1988).
10. J. E. Hart, On sideways diffusive instability, *J. Fluid Mech.* **49**, 279–288 (1971).
11. R. A. Wirtz and L. H. Liu, Numerical experiments on the onset of layered convection in a narrow slot containing a stably stratified fluid, *Int. J. Heat Mass Transfer* **18**, 1299–1305 (1975).
12. C. F. Chen, Onset of cellular convection in a salinity gradient due to a lateral temperature gradient, *J. Fluid Mech.* **63**, 563–576 (1974).
13. S. Thangam, A. Zebib and C. F. Chen, Double diffusive convection in an inclined fluid layer, *J. Fluid Mech.* **116**, 363–378 (1982).
14. C. F. Chen, D. G. Briggs and R. A. Wirtz, Stability of thermal convection in a salinity gradient due to lateral heating, *Int. J. Heat Mass Transfer* **14**, 57–65 (1971).
15. H. E. Huppert and J. S. Turner, Ice blocks melting into a salinity gradient, *J. Fluid Mech.* **100**, 367–384 (1980).
16. H. E. Huppert, R. C. Kerr and M. A. Halworth, Heating or cooling a stable compositional gradient from the side, *Int. J. Heat Mass Transfer* **27**, 1395–1401 (1984).
17. R. A. Wirtz, D. G. Briggs and C. F. Chen, Physical and numerical experiments on layered convection in a density stratified fluid, *Geophys. Fluid Dyn.* **3**, 265–288 (1972).
18. S. V. Patankar, *Numerical Heat Transfer and Fluid Flow*. McGraw-Hill, New York (1980).
19. J. W. Lee and J. M. Hyun, Double-diffusive convection in a rectangle with opposing horizontal temperature and concentration gradients, *Int. J. Heat Mass Transfer* **33**, 1619–1632 (1990).
20. J. M. Hyun and J. W. Lee, Double-diffusive convection in a rectangle with cooperating horizontal gradients of temperature and concentration, *Int. J. Heat Mass Transfer* **33**, 1605–1617 (1990).

21. J. Lee, M. T. Hyun and K. W. Kim, Natural convection in confined fluids with combined horizontal temperature and concentration gradients, *Int. J. Heat Mass Transfer* **31**, 1969–1977 (1988).
22. Y. Kamotani, L. W. Wang, S. Ostrach and D. J. Jiang, Experimental study of natural convection in shallow enclosures with horizontal temperature and concentration gradient, *Int. J. Heat Mass Transfer* **28**, 165–173 (1985).
23. R. A. Wirtz and C. S. Reddy, Experiments on convective layer formation and merging in a differently heated slot, *J. Fluid Mech.* **91**, 451–464 (1979).
24. J. M. Hyun and J. W. Lee, Numerical solutions for transient natural convection in a square cavity with different sidewall temperatures, *Int. J. Heat Fluid Flow* **10**, 146–151 (1989).

## DOUBLE DIFFUSION DEPENDANTE DU TEMPS DANS UN FLUIDE STABLE STRATIFIE AVEC CHAUFFAGE LATERAL

**Résumé**—On étudie numériquement la double diffusion dans un rectangle. Le fluide est initialement au repos avec un gradient solutal préexistant de stratification stable. Le mouvement est créé par une élévation brusque de température à une paroi laterale verticale. Ont été obtenues des solutions numériques des équations complètes de Navier–Stokes avec hypothèse du fluide de Boussinesq. Des analyses sont faites pour un large domaine de nombre de Rayleigh solutal $R_s$ et un nombre de Rayleigh thermique $R_t = 10^7$. On construit les profils verticaux de vitesse, de température, de concentration et de nombre de Nusselt, en délimitant l'influence de l'effet de flottement solutal relativement à l'effet thermique. Le comportement de l'écoulement est en bon accord qualitatif avec les visualisations expérimentales. La caractérisation du caractère fondamental de l'écoulement dans le régime supercritique ($Ra > Ra_c$) et subcritique ($Ra < Ra_c$), basée sur les observations expérimentales, est vérifiée par les résultats numériques. Les simulations numériques illustrent la différence quantitative de formation dans le temps de la structure lamellaire dans les régimes supercritique et subcritique. L'estimation antéricure de la valeur $Ra_c \cong 1{,}5 \times 10^4$ est trouvée être raisonnablement précise.

## ZEITABHÄNGIGE DOPPELDIFFUSION IN EINEM STABIL GESCHICHTETEN FLUID BEI SEITLICHER BEHEIZUNG

**Zusammenfassung**—Die doppelt-diffusive Konvektion in einer rechteckigen Anordnung wird numerisch untersucht. Das Fluid ist anfangs in Ruhe und besitzt einen stabil geschichteten Lösungsgradienten. Eine plötzliche Erhöhung der Temperatur der einen senkrechten Seitenwand führt zum Einsetzen der Bewegung. Der vollständige Satz der Navier–Stokes-Gleichungen wird unter Anwendung der Boussinesq-Approximation numerisch gelöst. Die Ergebnisse, welche einen weiten Bereich der Lösungs-Rayleigh-Zahl $R_s$ unter Verwendung der thermischen Rayleigh-Zahl $R_t = 10^7$ abdecken, werden eingehend analysiert. Die Entwicklung des Strömungs-, Temperatur- und Konzentrationsfeldes im Hohlraum wird grafisch dargestellt. Die senkrechten Profile der Geschwindigkeit, der Temperatur, der Konzentration und der örtlichen Nusselt-Zahl zeigen den relativen Einfluß des konzentrationsbedingten Auftriebs gegenüber dem thermischen Auftrieb. Das berechnete Verhalten der Strömung stimmt gut mit verfügbaren visuellen Strömungsbeobachtungen überein. Die Einteilung der Strömungsform in überkritische ($Ra > Ra_c$) und unterkritische Bereiche ($Ra < Ra_c$), die auf experimenteller Beobachtung fußt, wird durch die numerischen Ergebnisse in befriedigender Weise bestätigt. Die vorgelegte numerische Simulation bestätigt auch frühere Beobachtungen zum qualitativen Unterschied bei der zeitlichen Entwicklung der geschichten Struktur im überkritischen und im unterkritischen Bereich. Der Wert $Ra_c \cong 1{,}5 \times 10^4$ war früher überschlägig ermittelt worden, er wird durch die vorliegenden numerischen Ergebnisse als hinreichend genau bestätigt.

## НЕСТАЦИОНАРНАЯ ДИФФУЗИЯ ТЕПЛА И МАССЫ В УСЛОВИЯХ ПОПЕРЕЧНОГО НАГРЕВА ЖИДКОСТИ С УСТОЙЧИВОЙ СТРАТИФИКАЦИЕЙ

**Аннотация**—Численно исследуется конвекция с учетом диффузии тепла и массы в прямоугольной полости. Первоначально жидкость находится в состоянии покоя при наличии градиента растворенного вещества с устойчивой стратификацией. Движение вызывается резким ростом температуры у одной из вертикальных боковых стенок. Получены численные решения полных уравнений Навье–Стокса в приближении Буссинеска. С использованием теплового числа Рэлея $R_t = 10^7$ проведен анализ численных результатов, полученных в широком диапазоне изменений чисел Рэлея для растворенного вещества $R_s$. Представлены подробные графики, иллюстрирующие эволюцию полей течения, температуры и концентрации растворенного вещества в полост. Построены вертикальные профили скоростей температур, концентраций растворенного вещества и локальных чисел Нуссельта, описывающие взаимосвязь между подъемной силой из-за неоднородности концентрации и тепловым эффектом. Рассчитанные характеристики течения качественно согласуются с имеющимися экспериментальными данными по визуализации. Найденная из экспериментов классификация основных режимов течения на закритический ($Ra > Ra_c$) и докритический ($Ra < Ra_c$) удовлетворительно подтверждается численными результатами. Приведенное численное моделирование подтверждает также ранее сделанные наблюдения, иллюстрирующие качественное различие нестационарных картин образования слоистой структуры в закритическом и докритическом режимах. Анализ полученных численных результатов позволяет заключить, что предыдущая оценка значения $Ra_c \cong 1{,}5 \times 10^4$ является достаточно точной.